ORIGINAL PAPER

Fabrication of waste paper/graphene oxide three-dimensional aerogel with dual adsorption capacity toward methylene blue and ciprofloxacin

Fengjuan Yang[1] · Jinglin Zhang[1,2] · Tongyao Lin[1] · Liying Ke[1] · Langhuan Huang[1] · Sui-Ping Deng[1] · Jingxian Zhang[1] · Shaozao Tan[1] · Yongqiang Xiong[1] · Ming Lu[3]

Abstract

To effectively treat the pollutant in sewage, a new-type three-dimensional aerogel based on graphene oxide and waste paper was fabricated via simple mixing and freeze-drying processes. Therein, waste paper was activated in advance, and polyvinyl alcohol served as physical crosslinking agent. The results showed that the obtained aerogel with porous three-dimensional network structure exhibited good thermal stability. When it acted as adsorbent for treating organic dye (methylene blue) and antibiotic (ciprofloxacin), the adsorption process was explored. In single system, the pseudo-first-order and pseudo-second-order kinetic models were used to discuss the detail about the aerogel adsorbing pollutant. Moreover, the Langmuir and Freundlich adsorption models were applied to describe the equilibrium isotherms and calculate the isotherm constants. Thermodynamic results stated that the adsorption of pollutant onto aerogel was feasible and spontaneous. In binary system, the adsorption capacity of methylene blue by aerogel increased, while the adsorption capacity of ciprofloxacin by aerogel declined. The pseudo-second-order kinetics was consistent with the adsorption of pollutant by aerogel in such binary system. This study would provide a new boulevard to develop environmental, low-cost and high-efficiency adsorbent for removing pollutant from wastewater.

✉ Shaozao Tan
tsztan@jnu.edu.cn

✉ Yongqiang Xiong
yqxiong1978@163.com

✉ Ming Lu
7833610@qq.com

1 Guangdong Engineering and Technology Research Centre of Graphene-Like Materials and Products, Department of Chemistry, College of Chemistry and Materials Science, Jinan University, Guangzhou 510632, People's Republic of China

2 School of Light Industry and Materials, Guangdong Polytechnic, Foshan 528041, People's Republic of China

3 School of Chemistry and Materials Engineering, Huizhou University, Huizhou 516007, People's Republic of China

Graphical abstract
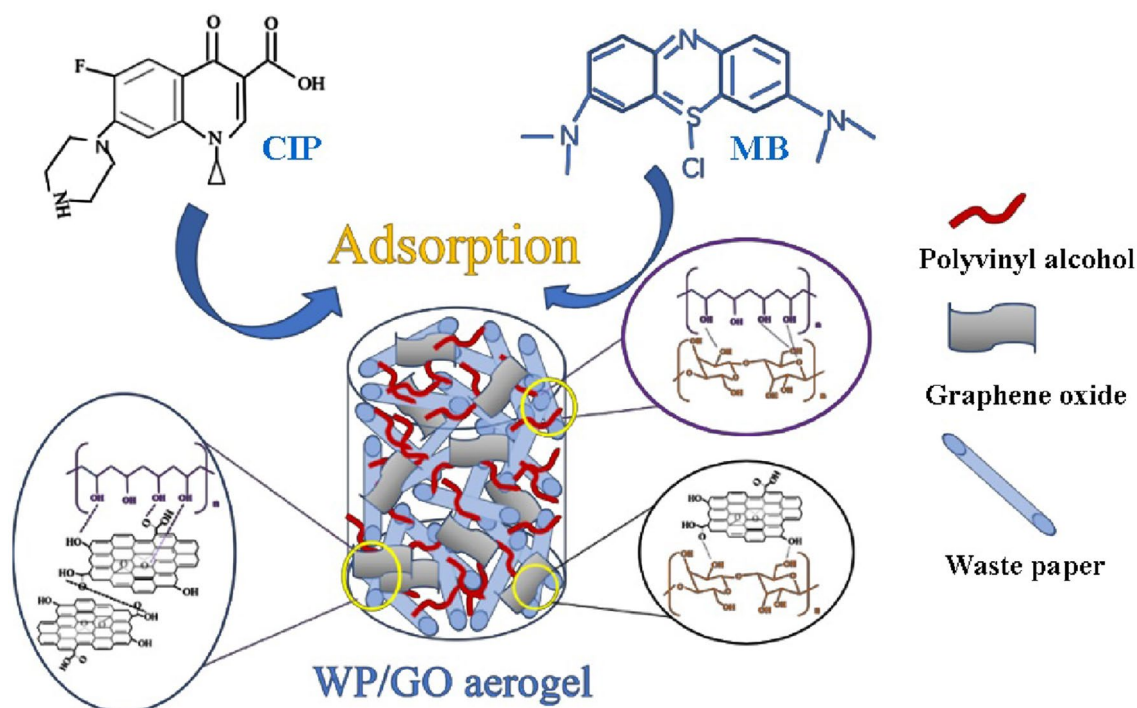
Introduction

In recent decades, various pollutants (e.g., organic dyes, antibiotics, etc.) have been introduced into the water system, seriously polluting water resource and adversely affecting human being, wildlife and local ecosystem [1, 2]. Owing to the rapid growth of textile industry and the corresponding mass production/use, organic dyes have been one of the main sources of severe water pollution. Methylene blue (MB), a commonly used organic dye, is considered to be the main type of water pollutant. It is a highly toxic and persistent compound with complex aromatic molecular structure [3]. Even at low concentration, the presence of organic dye in water is highly visible and undesirable. In addition, there is a growing trend in the consumption of antibiotics, many of which have been abandoned in water, soil and other environments, causing serious pollution. Ciprofloxacin (CIP) is an important fluoroquinolone antibiotic, which is widely distributed in surface water because of its long transformation time and low degradation efficiency [4], leading to the contamination of water and the toxicity to microorganism. With the extensive application of the above aromatic organics, they probably coexist in the industrial and agricultural wastewater system [5–7]. Consequently, environmental

problems will only be getting worse. To achieve the goal of sustainable development and green cleanliness, the treatment of diverse aromatic organics is a meaningful task. Although the coprocessing of organic dye and antibiotic is never widely studied, it is a promising method which can be applied in the large-scale application. Therefore, it is of great practical significance to effectively remove such single or multiple chemical pollutants from wastewater [8, 9]. So far, biodegradation, adsorption, coagulation–flocculation, membrane treatment and photocatalysis have been employed [10–16]. The demand for the pollutant removal technology is becoming higher and higher. Among different methods, adsorption is a feasible sewage treatment technology. It can be conducted under different conditions and has the advantages of simple use, flexibility, low cost and multi-purpose design [17–19].

As well known, the ideal adsorbent should have excellent comprehensive properties, such as high adsorption capacity, fast adsorption speed, large size, easy separation/recovery from suspension, simple desorption process and reusability [20]. At present, the common types of adsorbents include inorganic material [21], silver-based material [22], metal organic framework [23], porous organic framework (plastic optical fiber) [24], covalent organic framework [25], porous

aromatic framework [26], aerogel [27], etc. However, they have great differences in the fields of separation, recovery, adsorption, stability and cost. An adsorbent with good comprehensive performance is quite important for the adsorption method.

Among diverse adsorbent materials, graphene oxide (GO) is a promising candidate. The oxygen-containing groups (e.g., carboxyl, hydroxyl, carbonyl and epoxy groups) on the surface of GO can act as active sites for adsorbing various water pollutants [28]. Nevertheless, GO with two-dimensional nature has some shortcomings. For example, GO has poor structural stability in the water environment, which easily leads to the difficult recovery and secondary pollution [29]. To solve this predicament, the synthesis of three-dimensional GO is an effective approach. The fabrication of three-dimensional structure (e.g., sponge, aerogel and foam) can not only retain the inherent characteristic of GO, but also endow it with reusability in practical operation [30]. More importantly, the recovery operation based on such three-dimensional GO adsorbent can significantly reduce the release of GO nanoparticle into the environment [31]. As a rising carbon material, three-dimensional GO can possess abundant micropore/mesopore, providing sufficient adsorption site for pollutant. Furthermore, the π-conjugated structure and oxygen-containing group enable three-dimensional GO to be non-covalently/covalently connected with various functional materials, thereby enhancing the adsorption capacity [32]. Chen et al. [33] synthesized reusable three-dimensional agar/GO composite aerogel by vacuum freeze-drying method and exhibited its potential as adsorbent for MB. To date, many efforts have been made to manufacture an aerogel containing GO with good adsorption performance, which can be applied to effectively remove contaminant from wastewater.

On the other hand, with the development of adsorption technology, more and more waste biomass materials are processed and used as adsorbents for treating pollutants [34–36]. The utilization of such biomass is eco-friendly, low-cost, renewable and conducive to waste recycling, which has attracted extensive research interest. Waste paper, which is mainly from wood pulp and cotton, is composed of 90–99% cellulose and has a mesh frame structure [37, 38]. With the characteristics of wide availability, low cost, light weight and recyclability, it has a good application prospect. The cellulose in waste paper is rich in carbon, pore structure and functional groups like carboxyl and hydroxyl [39]. Waste paper is usually used as raw material for cellulose-based aerogel with excellent hydrophobicity [40]. Even so, the aerogel made from waste paper has relatively low adsorption capacity when directly applied as adsorbent. Thus, some valid methods like modification and compound have been proposed to improve this characteristic, aiming to obtain high adsorption capacity toward contaminant [41, 42].

In this work, given the above considerations, we proposed a new-type three-dimensional aerogel based on GO and waste paper via simple mixing and freeze-drying processes. Therein, waste paper was activated in advance, and poly-vinyl alcohol (PVA) acted as physical crosslinking agent. To the best of our knowledge, a few relevant published reports were available. The structure, morphology, thermal stability, pore size distribution and specific surface area of the obtained aerogel were explored. Moreover, the aerogel served as adsorbent for adsorbing organic dye (MB) and antibiotic (CIP). The effects of adsorption time, mass ratio, temperature and pH on the adsorption process were investigated. The mono-adsorption and co-adsorption behaviors of pollutants on aerogel were also studied by kinetic and/or thermodynamic analyses. This study would provide a new boulevard to develop environmental, low-cost and high-efficiency adsorbent for the treatment of pollutant in wastewater.

Experimental section

Materials

Graphite powder (spectral pure) and phosphorus pentoxide (P_2O_5) were purchased from Shanghai Lingfeng Chemical Reagent Co., Ltd. Sulfuric acid (H_2SO_4, 98%) and hydrogen peroxide (H_2O_2) were purchased from Tianjin Fuchen Chemical Reagent Co., Ltd. Potassium permanganate ($KMnO_4$), sodium hydroxide (NaOH), urea and ethanol were supplied by Dongguan Chemical Reagent Co., Ltd. Polyvinyl alcohol (PVA) was provided by Shanghai McLean Biochemical Technology Co., Ltd. All other reagents and solvents were obtained from commercial suppliers. All aqueous solutions were prepared with ultrapure water (> 18 MΩ) through a Milli-Q Plus system (Millipore).

Preparation of sample

GO was synthesized via oxidizing natural graphite powder based on modified Hummers method as presented by previous literatures [43, 44].

The activation treatment of waste paper was conducted as follows. First, 100 mL of NaOH/urea aqueous solution (7 wt%/12 wt%) was kept in the refrigerator at − 18 °C for 1 h. Then, 4.000 g of waste paper was added into the above solution and the mixture was stirred at room temperature for 10 min. Afterward, 100 mL of ethanol was added and the compound was kept at room temperature for 24 h. Consequently, the obtained white powdery solid was washed with deionized water until pH 7 and was freeze-dried for 48 h. The corresponding product was named as activated waste paper (WP).

After that, 0.01 g of WP was added into 10 mL of deionized water and the mixture was stirred for 1 h. Then, a certain amount of GO was put in. After ultrasonic treatment for 0.5 h and stir for another 2 h, 0.8 g of 5% PVA solution was mixed. Continuing to stir for 0.5 h, the compound was poured into a 12-well plate mold and was frozen below 0 °C for 8 h. Finally, WP/GO aerogel with three-dimensional network was acquired by freeze-drying treatment. Therein, the aerogel with different mass ratio was designated as WP/GO$_{x:y}$, where x represented the mass of WP and y represented the mass of GO in the aerogel.

Characterizations

Fourier transform infrared (FTIR) spectra between 500 and 4000 cm^{-1} were obtained on a Nicolet 6700 spectrometer. Transmission electron microscopy (TEM) images were observed by using a JEOL JEM-2100F transmission electron microscope. Scanning electron microscope (SEM, FlexSEM1000el Hitachi, Japan) was applied to observe the surface morphology of as-prepared sample; the sample was coated with a thin layer of gold before analysis. Thermogravimetric analysis (TGA) was run on a SDT Q600 V20.9 Build 20 thermogravimetric analyzer at a heating rate of 10 °C/min from room temperature to 800 °C in nitrogen flow. X-ray diffraction (XRD) pattern was recorded on a diffractometer (D/max-1200) using graphite monochromatic Cu K_α radiation ($\lambda = 0.1541$ nm) at a generator voltage of 36 kV and a current of 20 mA; measurement was conducted within a 2θ range of 5.0°–80.0° at a scanning rate of 2°/min. The Brunauer–Emmett–Teller (BET) surface area was determined from nitrogen adsorption and desorption isotherm data obtained at 77 K with a constant-volume adsorption apparatus (Mmk-TriStar3000). Raman spectra were obtained on a Renishaw RM2000 Raman spectrometer.

Adsorption test toward MB

In single system, 0.02 g of WP/GO$_{1:3}$ aerogel was added into 40 mL of MB solution with a series of concentration. Then, the mixture was oscillated in a constant-temperature water bath shaker at 25 °C for a certain time. After that, 1 mL of supernatant liquid was taken into a 10-mL centrifuge tube using pipette and was diluted ten times for analysis. Specifically, the absorbance at $\lambda_{max} = 664$ nm (A_{664}) was measured with a Hitachi 330 UV–Vis spectrophotometer. The concentration of MB could be calculated according to the linear equation of standard curve ($y = 0.1703x + 0.0793$, $R^2 = 0.9993$).

Adsorption test toward CIP

In single system, 0.02 g of WP/GO$_{1:3}$ aerogel was added into 40 mL of CIP solution with a series of concentration. Then, the mixture was oscillated in a constant-temperature water bath shaker at 25 °C for a certain time. After that, 1 mL of supernatant liquid was taken into a 10-mL centrifuge tube using pipette and was diluted ten times for analysis. Specifically, the absorbance at $\lambda_{max} = 273$ nm (A_{273}) was measured with a Hitachi 330 UV–Vis spectrophotometer. The concentration of CIP could be calculated according to the linear equation of standard curve ($y = 0.0965x - 0.00311$, $R^2 = 0.9991$).

Adsorption test toward MB and CIP

During the adsorption test in binary system, the mixture of 50 mg/L MB solution and 100 mg/L CIP solution was prepared. Next, 40 mL of the above mixture and 0.02 g of WP/GO$_{1:3}$ aerogel were put into a conical flask. The conical flask was placed in an oscillating box, and the intermittent adsorption test was conducted at a speed of 150 r/min. The procedures for adsorption and analysis were kept the same as described above.

At equilibrium, the adsorption capacity and removal rate were determined by the following equations:

$$q_e = \frac{(C_0 - C_e)V}{M} \tag{1}$$

$$\eta = \frac{(C_0 - C_e)}{C_0} \times 100 \tag{2}$$

where q_e was the adsorption capacity (mg/g), η was the removal rate (%), V was the volume of solution (L), C_0 was the initial concentration of solution (mg/L), C_e was the equilibrium concentration of solution (mg/L), and M was the mass of adsorbent (g), respectively.

The linear form of Langmuir isotherm model was given by:

$$\frac{C_e}{q_e} = \frac{1}{Q_{max}K_L} + \frac{C_e}{Q_{max}} \tag{3}$$

where K_L (L/mg) was the Langmuir constant consist with the rate of adsorption and Q_{max} (mg/g) was the Langmuir maximum removal capacity of pollutant per unit mass of adsorbent.

The logarithmic form of Freundlich isotherm model was given by:

$$\ln q_e = \ln K_F + \frac{1}{n} \ln C_e \tag{4}$$

where n and K_F were defined as the Freundlich constants, indicating the favorableness of the adsorption process and the removal capacity of the adsorbent, respectively.

The thermodynamic model of pollutant adsorption on adsorbent was evaluated by the thermodynamic parameters including the changes in entropy (ΔS), free energy (ΔG) and enthalpy (ΔH). All of the thermodynamic parameters were calculated according to the equations:

$$\ln(K_d) = \frac{\Delta S}{R} - \frac{\Delta H}{RT} \qquad (5)$$

$$\Delta G = -RT \ln(K_d) \qquad (6)$$

$$K_d = \frac{(C_0 - C_e)}{C_e} \times \frac{V}{M} \qquad (7)$$

where K_d was the distribution coefficient of adsorption process, R was the universal gas constant, and T was the temperature (K).

The pseudo-first-order kinetic model was used for low concentration of solute, which was written by:

$$\ln(q_e - q_t) = \ln q_e - k_1 t \qquad (8)$$

where q_t was the pollutant amount adsorbed at time t (mg/g), q_e was that adsorbed at the equilibrium (mg/g), and k_1 was the rate constant of pseudo-first-order equation.

The pseudo-second-order equation was suitable for the amount of the solute adsorbed on the surface of adsorbent and the dosage adsorbed at equilibrium, which could be stood for the following equation:

$$\frac{t}{q_t} = \frac{1}{k_2 q_e^2} + \frac{t}{q_e} \qquad (9)$$

where k_2 was the rate constant of pseudo-second-order equation, while t, q_e and q_t had the same meanings as those in pseudo-first-order equation.

Results and discussion

Basic characterizations

The XRD patterns of GO, WP, PVA and WP/GO$_{1:3}$ aerogel are given in Fig. 1a. For GO, a strong diffraction peak appeared at $2\theta = 10.44°$, corresponding with the (002) interlayer spacing of 0.79 nm, which was much larger than that of the original graphite (ca. 0.34 nm). It was because of the presence of covalently bonded oxygen-containing functional group and the amount of absorbed moisture [45]. This result indicated that there were many oxygen-containing functional groups on its surface, revealing the successful oxidation of the original graphite powder. For WP, a characteristic diffraction peak of cellulose was observed at $2\theta = 22.25°$. For PVA, the characteristic diffraction peaks at $2\theta = 19.4°$ and $40.8°$ were found, corresponding to the (101) and (200) reflections [46, 47]. For WP/GO$_{1:3}$ aerogel, a diffraction peak at $2\theta = 6.26°$ appeared, which belonged to the characteristic peak of GO that had shifted to the left. According to the Bragg equation, it might be because GO was throughout supported by cellulose in the synthetic aerogel, which increased the interlayer spacing of GO. Moreover, the characteristic peak of PVA shifted to $2\theta = 15.67°$ and the intensity of diffraction peak reduced, which might be ascribed to the decrease in the crystallinity of PVA in the aerogel. The characteristic peak of cellulose also emerged at $2\theta = 22.25°$. These results implied that WP/GO$_{1:3}$ aerogel had been successfully prepared.

FTIR spectroscopy could reflect the functional group contained in the substance. Figure 1b shows the FTIR spectra of GO, WP, PVA and WP/GO$_{1:3}$ aerogel. For PVA, a broad peak appeared at 3416 cm^{-1}, which could be ascribed to the O–H stretching vibration. In addition, the peaks at 2942, 1452 and 1089 cm^{-1}, respectively, corresponded to the characteristic vibration frequencies of C–H, C–O and C–C and the bending vibration of C–H [48]. For GO, the characteristic peaks of various oxygen-containing functional groups were observed, including –OH (3420–3606 cm^{-1}), –COOH (1722 cm^{-1}) and C=C (1619 cm^{-1}). It indicated the successful preparation of GO [49]. For WP, the peaks at 3354, 1374 and 2899 cm^{-1} were assigned to the stretching vibration of −OH, bending vibration of −OH and asymmetry/symmetry stretching vibration of C–H, respectively. Furthermore, the peaks at 1118, 1166, 1427 and 1054 cm^{-1} belonged to the absorption peaks of cellulose I crystal, which were related to the antisymmetric bridge stretching of C–O, symmetrical shear of –CH$_2$ in pyridine ring and skeleton vibration of C–O. For WP/GO$_{1:3}$, it could be found that the characteristic peaks of WP and GO arose. Specifically, the peaks at 1427 and 1054 cm^{-1} were the characteristic peaks of WP, while the peaks at 1722 and 1619 cm^{-1} were the characteristic peaks of GO. These results suggested the successfully synthesis of WP/GO$_{1:3}$ aerogel, which were consistent with the XRD results.

As shown in Fig. 1c, the Raman spectrum of GO gave two prominent peaks at 1350 and 1580 cm^{-1}, corresponding to the characteristic D and G bands, respectively [50]. D band represented the C sp^3 atom of the K-point phonon, and G band represented the C sp^2 atom of the E_{2G} phonon. The appearance of D band indicated that C=C in graphite layer was destroyed due to the oxidation treatment [51]. Generally speaking, the intensity ratio of the D band and G band (I_D/I_G) in the Raman spectrum could be used to estimate the degree of disorder in carbon material. The considerable I_D/I_G value of GO (0.90) stated high concentration of structure defect on
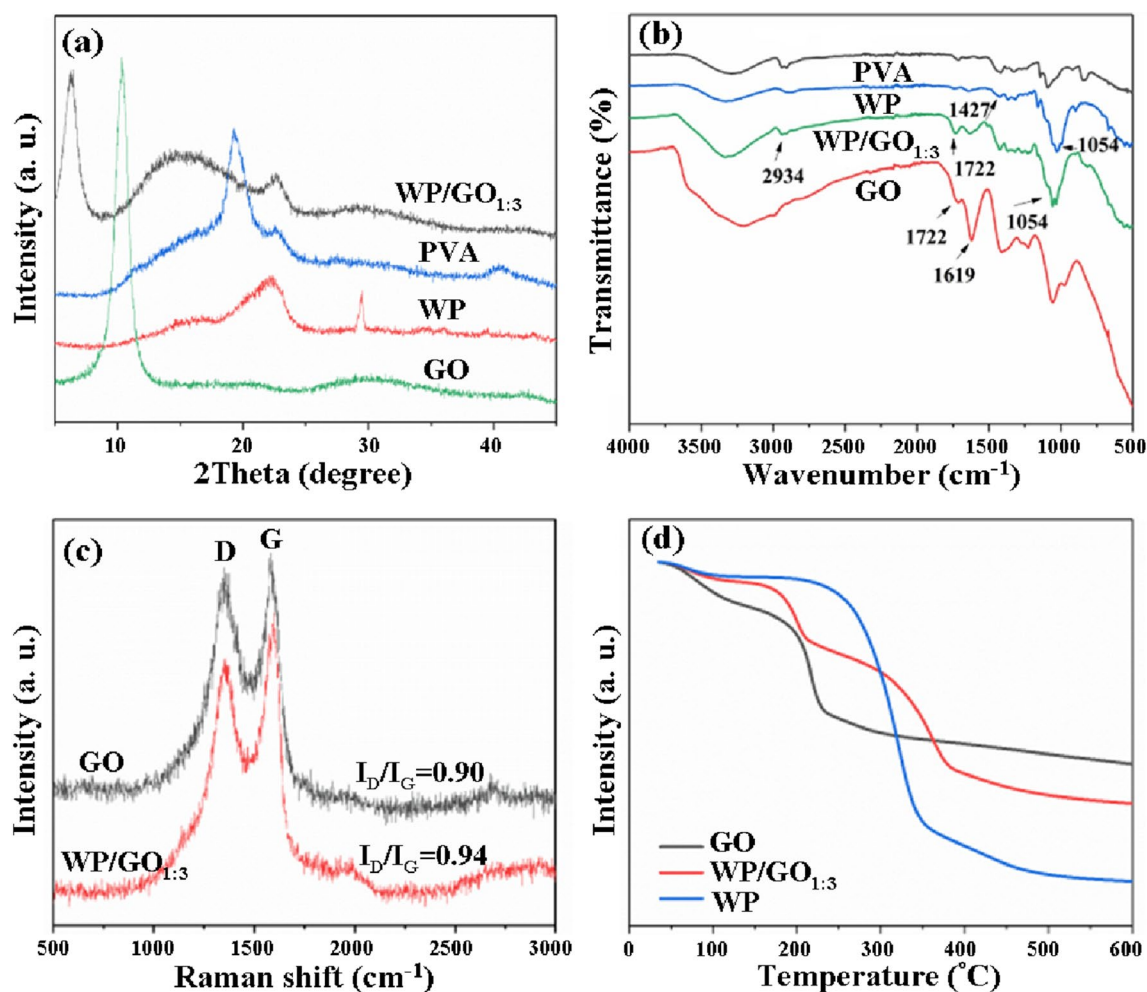
Fig. 1 **a** XRD patterns of GO, WP, PVA and WP/GO1:3 aerogel. **b** FTIR spectra of GO, WP, PVA and WP/GO1:3 aerogel. **c** Raman spectra of GO and WP/GO1:3 aerogel. **d** TGA curves of GO, WP and WP/GO1:3 aerogel

the surface of GO, which was ascribed that a large number of oxygen-containing functional groups were attached to the GO surface. The presence of these oxygen-containing groups made GO disperse easily in water and form good interaction with polar cellulose molecule. For WP/GO$_{1:3}$ aerogel, the I_D/I_G value increased to be 0.94, indicating that the physical crosslinking between the WP and GO slightly increased the defect and reduced the order of aerogel. It might be because some oxygen-containing functional groups of GO fell off or participated in the crosslinking process [52].

The thermal stability of aerogel was a key factor for its practical application. To explore the thermal property of the obtained aerogel, TGA was carried out and the results are shown in Fig. 1d. For GO, the weight loss at 100 °C was mainly due to the evaporation of water absorbed on the sample during the preparation process. The weight loss (ca. 20 wt%) from 150 to 200 °C was attributed to the decomposition of the oxygen-containing functional groups on the surface of GO. The high water content (ca. 10 wt%) of GO

signified that many oxygen-containing functional groups were bonded to the plane of GO, which would facilitate the adsorption of pollutant. For WP, there was a great weight loss at 300 °C, which was caused by the thermal degradation of cellulose [53]. For WP/GO$_{1:3}$ aerogel, the weight loss at 200 °C might be due to the decomposition of the oxygen-containing groups in GO. Besides, the weight loss (ca. 30 wt%) in the range of 200–400 °C was owing to the decomposition of cellulose. It was worth noting that the addition of GO was conducive to improve the thermal stability of WP. The favorable thermal stability of the three-dimensional network aerogel might be ascribed to the strong interaction between cellulose and GO, leading to the formation of network crosslinking structure of aerogel.

The morphological characteristics of GO, WP and WP/GO$_{1:3}$ aerogel were investigated using SEM and TEM. In Fig. 2a, d, GO displayed a sheet-like morphology with characteristically wrinkled architecture. In Fig. 2b, e, it could be seen that the cellulose contained in WP was tubular with
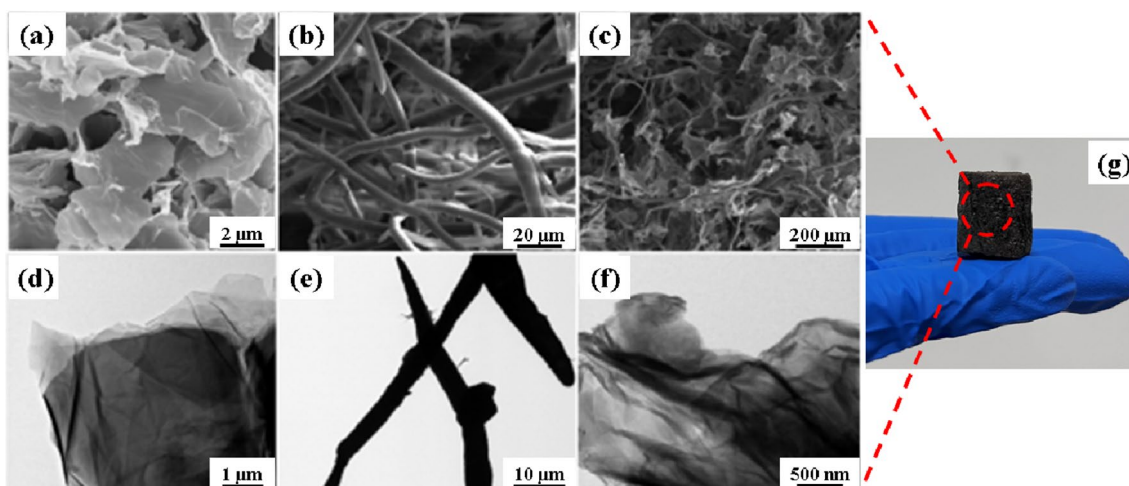
Fig. 2 SEM images of **a** GO, **b** WP and **c** WP/GO$_{1:3}$ aerogel. TEM images of **d** GO, **e** WP and **f** WP/GO$_{1:3}$ aerogel. **g** Photograph of WP/GO$_{1:3}$ aerogel

smooth surface and uniform size. Moreover, the diameter of cellulose was ca. 4 μm. Figure 2c exhibits that the cellulose in WP was inserted through the GO sheet structure. Further, small lamellar GO was attached to the cellulose, making the surface of cellulose become rough. The FEM image of WP/GO$_{1:3}$ aerogel (Fig. 2f) also presented that the tubular cellulose was combined with the sheet-layer GO, forming a porous three-dimensional network aerogel, which was beneficial for the adsorption of MB and CIP. Figure 2g unveils the typical photograph of WP/GO$_{1:3}$ aerogel.

The porosity and specific surface area of sample were measured by BET data based on nitrogen adsorption/desorption isotherm. As shown in Fig. 3, the specific surface areas of WP and WP/GO$_{1:3}$ aerogel were 65.10 and 8.64 cm^2/g. Obviously, the specific surface area of WP/GO$_{1:3}$ aerogel

was much less than that of WP, which might be because of the aggregation of GO lamellar structure and the penetration of WP into GO sheet. According to Fig. 3b, the nitrogen adsorption/desorption behavior of WP/GO$_{1:3}$ aerogel was the characteristic type IV with H3 hysteresis isothermal loop, indicating the existence of mesoporous structure in WP/GO$_{1:3}$ aerogel. From the pore size distribution diagram (*inset* in Fig. 3b), it could be known that the pore size of WP/GO$_{1:3}$ aerogel was in the range of 2 and 10 nm, which was slightly larger than that of WP (*inset* in Fig. 3a). These results proved that WP/GO$_{1:3}$ aerogel had mesoporous structure. In summary, WP/GO$_{1:3}$ aerogel with hydrophilic functional group and mesoporous structure could provide sufficient adsorption site for pollutant, meaning that WP/GO$_{1:3}$ aerogel probably possessed good adsorption performance.
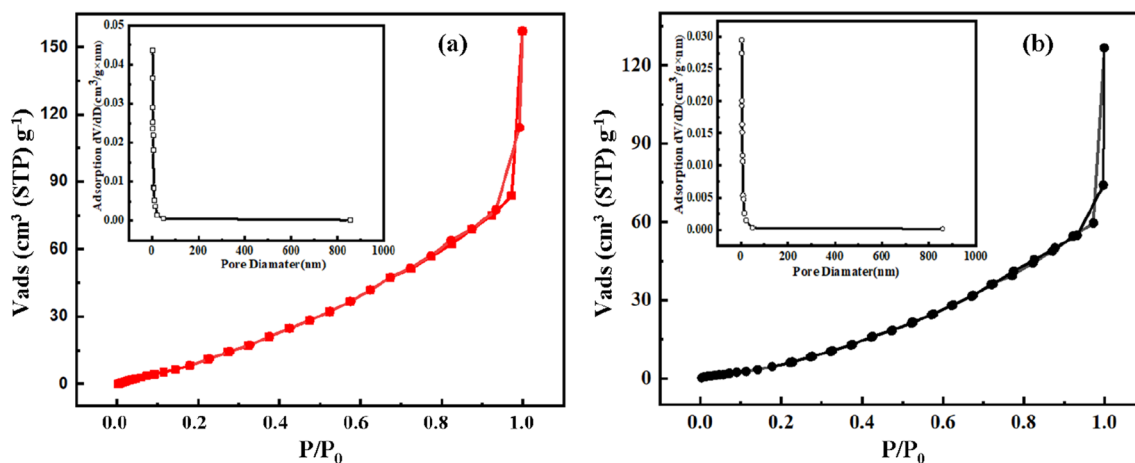

Fig. 3 Nitrogen adsorption/desorption isotherms of **a** WP (the *inset* was BJH pore size distribution) and **b** WP/GO$_{1:3}$ aerogel (the *inset* was BJH pore size distribution)

Adsorption kinetics analysis of single system

The adsorption processes of MB and CIP on WP/GO$_{1:3}$ aerogel were fitted with different kinetic models, and the experimental data of kinetic models for MB and CIP were calculated by the pseudo-first-order and pseudo-second-order models (Fig. 4 and Table 1). According to the correlation coefficients, the experimental data were more fitted to the pseudo-second-order model ($R^2 > 0.99$) than the pseudo-first-order model. Table 1 demonstrates that the $q_{e,cal}$ values of MB and CIP were more closer to the $q_{e,exp}$ values

of MB and CIP in the pseudo-second-order model than in the pseudo-first-order model. These outcomes were consistent with the previous literature [54]. It indicated that the pseudo-second-order kinetics would be more suitable for the adsorption processes of MB and CIP by WP/GO$_{1:3}$ aerogel, suggesting that the adsorption process involved chemical adsorption.

In order to study the interaction between MB/CIP and WP/GO$_{1:3}$ aerogel within the adsorption process, FTIR analysis was carried out. By comparing the FTIR spectra of WP/GO$_{1:3}$ aerogel before and after adsorption of
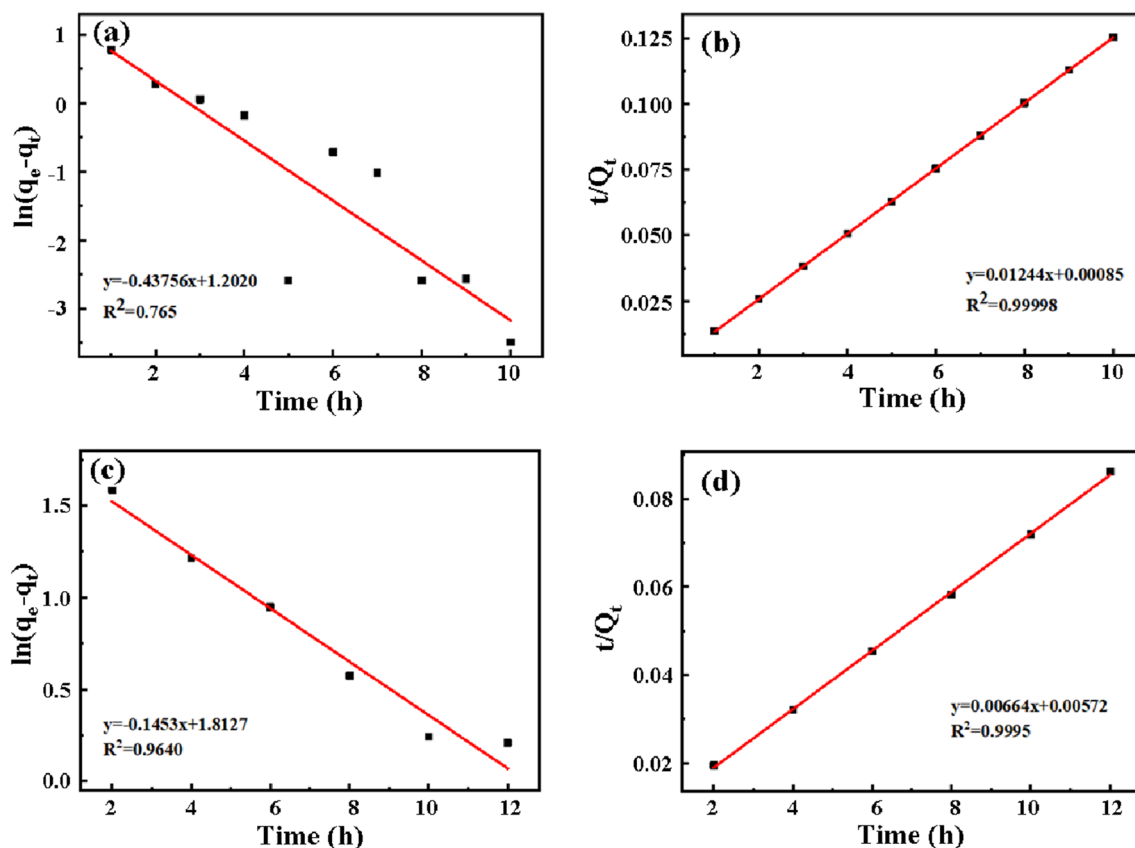

Fig. 4 **a** Pseudo-first-order and **b** pseudo-second-order plots for the adsorption of MB by WP/GO$_{1:3}$ aerogel. **c** Pseudo-first-order and **d** pseudo-second-order plots for the adsorption of CIP by WP/GO$_{1:3}$ aerogel

Table 1 Adsorption kinetic parameters for the adsorption of MB and CIP by WP/GO$_{1:3}$ aerogel

Temperature (K)	Pollutant	Pseudo-first-order model				Pseudo-second-order model		
		$q_{e,exp}$ (mg/g)	k_1 (1/h)	R^2	$q_{e,cal}$ (mg/g)	k_2 (mg/g/h^2)	R^2	$q_{e,cal}$ (mg/g)
298	MB	20.18	0.5343	0.983	77.84	0.0541	0.99993	79.68
	CIP	159.07	0.100	0.843	5.88	0.0921	0.99995	148
308	MB	5.79	0.5156	0.8788	79.496	0.2463	0.99999	79.87
	CIP	142.28	0.1931	0.7745	8.302	0.0602	0.99994	147.65
318	MB	15	1.007	0.765	79.714	0.1821	0.99998	80.38
	CIP	139.36	0.3346	0.9640	65.01	0.0077	0.9995	149.60

CIP (Fig. 5a), the characteristic peaks between 3300 and 3700 cm^{-1} enhanced and broadened, which might be due to the introductions of N–H and O–H functional groups and H–F hydrogen bond after the adsorption of CIP. Besides, new characteristic peaks appeared at 1614 and 1412 cm^{-1}, corresponding to the benzene ring skeleton vibration and C–F stretching vibration of CIP, respectively. The characteristic peak at 1275 cm^{-1} corresponded to the C–O stretching vibration peak in the FTIR spectrum of CIP. By comparing the FTIR spectra of WP/GO$_{1:3}$ aerogel before and after adsorption of MB (Fig. 5b), the peak at 3400 cm^{-1} broadened. In addition, new peaks observed at 1590, 1397 and 1332 cm^{-1} were ascribed to the characteristic peaks in the FTIR spectrum of MB. The peaks at 1141 and 1036 cm^{-1} were attributed to the C–S stretching vibration.

To further explore the microstructure change caused by the interaction between MB and WP/GO$_{1:3}$ aerogel, it was also characterized by FTIR technique (Fig. 5c, d). As the adsorption time passed, the characteristic peak of –OH at

3400 cm^{-1} gradually became wider and stronger. Apparently, the intensities of peaks at 1590, 1397 and 1322 cm^{-1} showed slight changes as well. These peaks belonged to the skeleton vibration of benzene ring, stretching vibration of C–H on the methyl group, in-plane torsional vibration of benzene ring skeleton and symmetrical bending vibration of C–H. Therefore, the adsorption process was possibly dominated by chemical action (hydrogen bonding and π–π conjugation), which was in accordance with the results of adsorption kinetics analysis. The adsorption capacity was proportional to the number of active site.

Adsorption isotherm model of single system

Generally speaking, the correlation coefficient (R^2) was used as a measure of fitness. R^2 value closer to 1 would indicate better adaptability to the corresponding isotherm equation. In Fig. 6a, b, the adsorption of MB by WP/GO$_{1:3}$ aerogel was more in line with the Langmuir
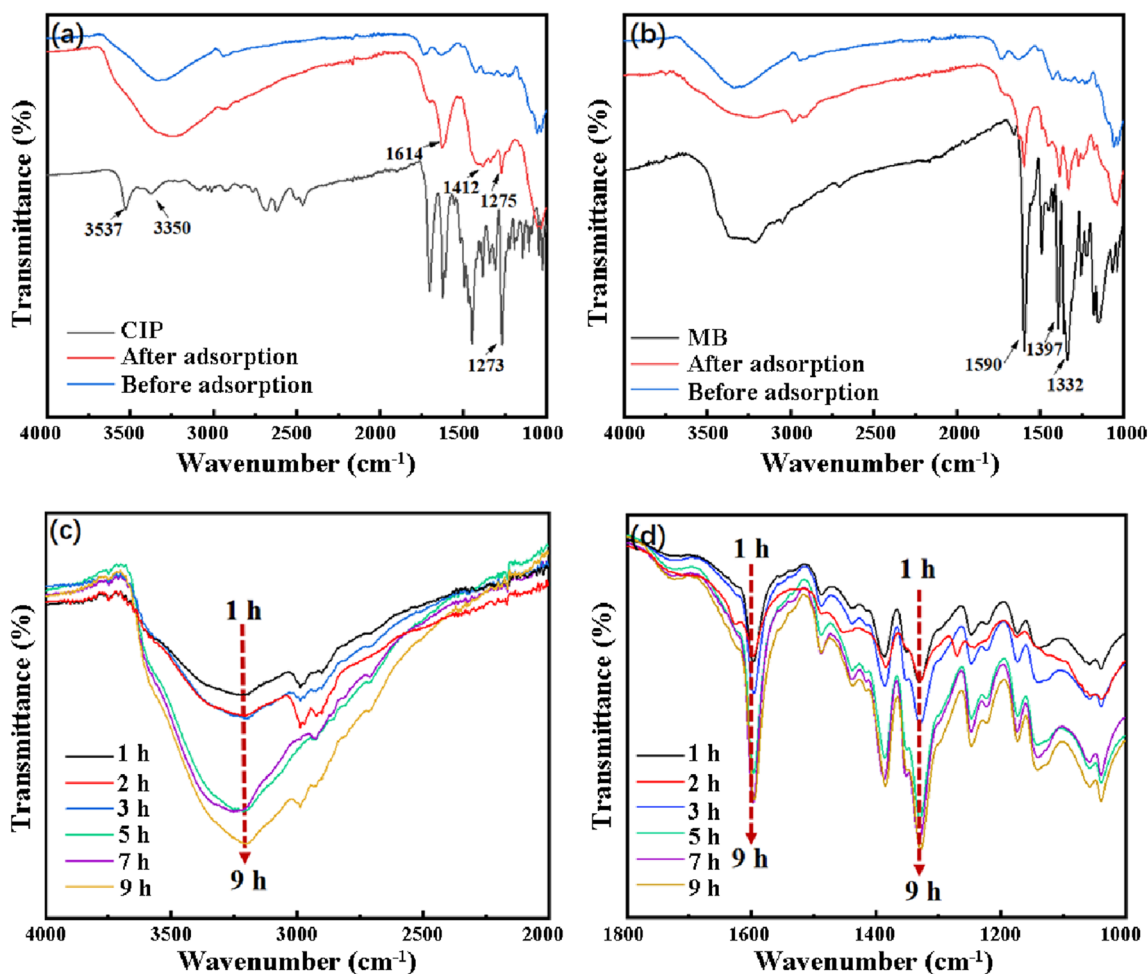

Fig. 5 FTIR spectra of WP/GO$_{1:3}$ aerogel before and after adsorption of **a** CIP and **b** MB. **c**, **d** FTIR spectra of WP/GO$_{1:3}$ aerogel adsorbing MB for different time
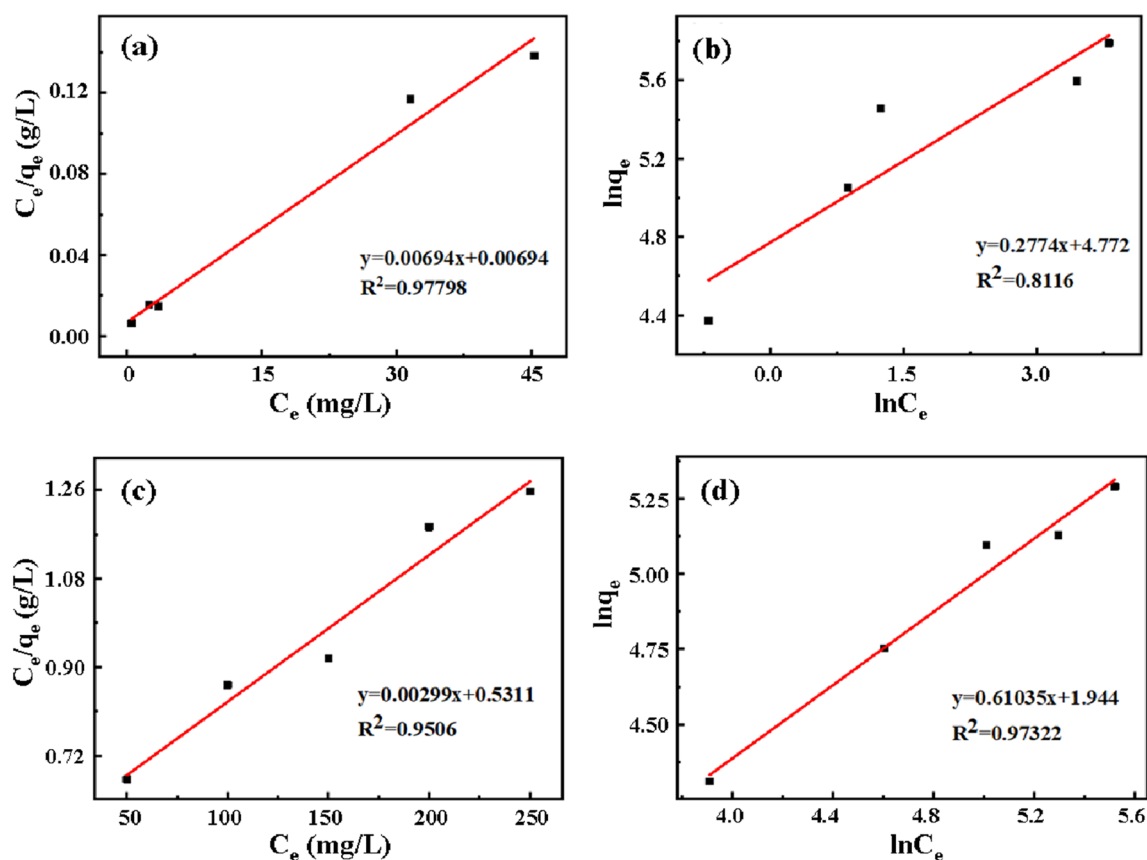
Fig. 6 **a** Langmuir and **b** Freundlich plots of the adsorption of MB by WP/GO$_{1:3}$ aerogel. **c** Langmuir and **d** Freundlich plots of the adsorption of CIP by WP/GO$_{1:3}$ aerogel

isotherm model since its R^2 value was closer to 1, presenting the single-layer homogeneous interface adsorption. In Fig. 6c, d, the adsorption of CIP by WP/GO$_{1:3}$ aerogel was more coincided with the Freundlich isotherm model because its R^2 value was closer to 1. Hence, the adsorption process of CIP could be explained as major multilayer adsorption and partial single-layer adsorption. In Table 2, the fitting constant (n) values in the Freundlich isotherm model were both less than 10, showing that the adsorption process was spontaneous. The adsorption constant (K_L) values were both in the range of 0 to 1, exhibiting that the adsorption of MB and CIP on aerogel was favorable [55].

Adsorption thermodynamic analysis of single system

Figure 7 displays that higher temperature was conducive to more adsorption of MB and CIP. In Table 3, the positive values of ΔH reflected the endothermic characteristics of the adsorption processes of MB and CIP [56]. Meanwhile, the positive values of ΔS affirmed that the affinity of aerogel for pollutant and the degree of freedom at solid–liquid interface increased [57]. At there given temperatures, the negative values of ΔG manifested that the adsorption of MB or CIP on WP/GO$_{1:3}$ aerogel was a spontaneous process [58]. For MB or CIP, the following relationship was satisfied: $\Delta H < T \cdot \Delta S$. Consequently, this binding reaction between pollutant and aerogel was mainly driven through entropy caused by hydrophobic interaction [59].

Table 2 Langmuir and Freundlich isotherm constants for the adsorptions of MB and CIP by WP/GO$_{1:3}$ aerogel

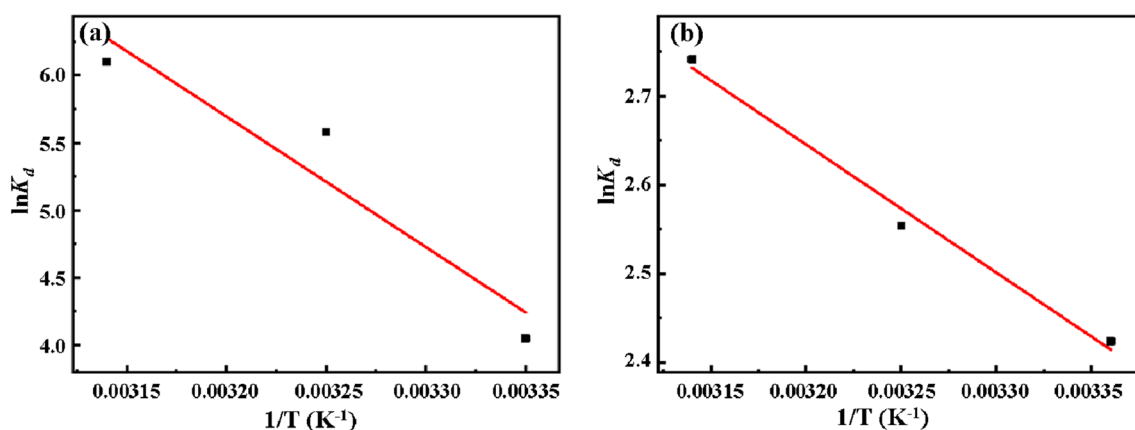| Pollutant	Langmuir			Freundlich		
	K_L (L/mg)	q_{max} (mg/g)	R^2	K_F (mg/g)/(L/mg)	n	R^2
MB	0.446	322.58	0.97798	118.15	3.605	0.8116
CIP	0.00563	144.45	0.9506	6.9866	1.64	0.97322

Fig. 7 Thermodynamic fitting curves for the adsorption of **a** MB and **b** CIP by WP/GO$_{1:3}$ aerogel

Table 3 Thermodynamic parameters for the adsorption of MB and CIP by WP/GO$_{1:3}$ aerogel at different temperatures

Pollutant	Temperature (K)	ΔG (kJ/mol)	ΔH (kJ/mol)	ΔS (J/mol/K)
MB	298	− 10.356	80.462	304.87
	308	− 14.288		
	318	− 15.783		
CIP	298	− 6.79	11.99	60.35
	308	− 6.54		
	318	− 6.41		

Effect of adsorption time, mass ratio and pH on adsorption process

Figure 8A, b reveals the effect of WP/GO aerogel with different mass ratio on the time-dependent adsorption of MB and CIP. From Fig. 8a, the adsorption of MB by WP/GO aerogel reached saturation (i.e., adsorption equilibrium) after 5 h. When the mass ratio of WP to GO was 1:3, the adsorption capacity of MB could reach the maximum (i.e., 80 mg/g). From Fig. 8b, the adsorption of CIP by WP/GO aerogel reached equilibrium after 8 h. The adsorption equilibrium time was quite short, and the adsorption amount achieved 158 mg/g. When the mass ratio of WP to GO was 1:3, the adsorption capacity of CIP could attain the maximum as well. So, WP/GO aerogel with 1:3 mass ratio of WP to GO (i.e., WP/GO$_{1:3}$ aerogel) was considered to be optimized and was used in other experiments.

On the other hand, pH was the most relevant parameter for the adsorption process. Especially for cationic dye, it was well known that due to the competition between excess H$^+$ and dye molecule, the adsorption of dye on the solid surface was limited under acidic condition. As shown in Fig. 8c, there was a lot of H$^+$ in the solution when the pH was low,

which inhibited the adsorption of MB on WP/GO$_{1:3}$ aerogel. With the pH value raised, the adsorption capacity gradually increased. When the solution was alkaline, the adsorption capacity continued to rise, indicating that the adsorption of MB mainly depended on the chemical adsorption of oxygen-containing functional group in WP/GO$_{1:3}$ aerogel.

Whether the organic compound would exist in a protonated or de-protonated form depended on the pH of solution and the dissociation constant (pKa) of organic compound. When the pH of solution was less than pKa, the organic compound usually existed in a positively charged protonated form, so the cationic form of target compound was dominant in the solution. If the pH of solution was greater than pKa, the surface functional group of compound was partially or completely de-protonated. In this case, the anionic form of target compound was dominant in the solution. Under the above two conditions, the interaction between target compound and adsorbent was unfavorable because of the electrostatic repulsion.

CIP was a zwitterion with an acidic pKa of 6.43 and a basic pKa of 8.9. When the pH value was less than 6.43, CIP existed in the form of cation. When the pH value was greater than 8.9, CIP existed in the form of anion. When the pH value was between them, CIP existed in the form of zwitterion. Moreover, affecting by the hydrophobic interaction, CIP tended to be adsorbed due to its low solubility [60]. This low solubility region was in the pH region of 5.90–8.89, where the adsorbate was electrostatically neutral and existed in the form of zwitterion. In a word, the pH of solution determined the existence form of CIP, affecting the adsorption amount of CIP on WP/GO$_{1:3}$ aerogel (Fig. 8d). As the pH value increased from 3 to 6, the adsorption amount of CIP slowly increased. If the pH value increased to 10, the adsorption rate of CIP gradually reduced. The reason might be that the adsorption affinity between CIP and adsorbent decreased significantly with the solution gradually became alkaline
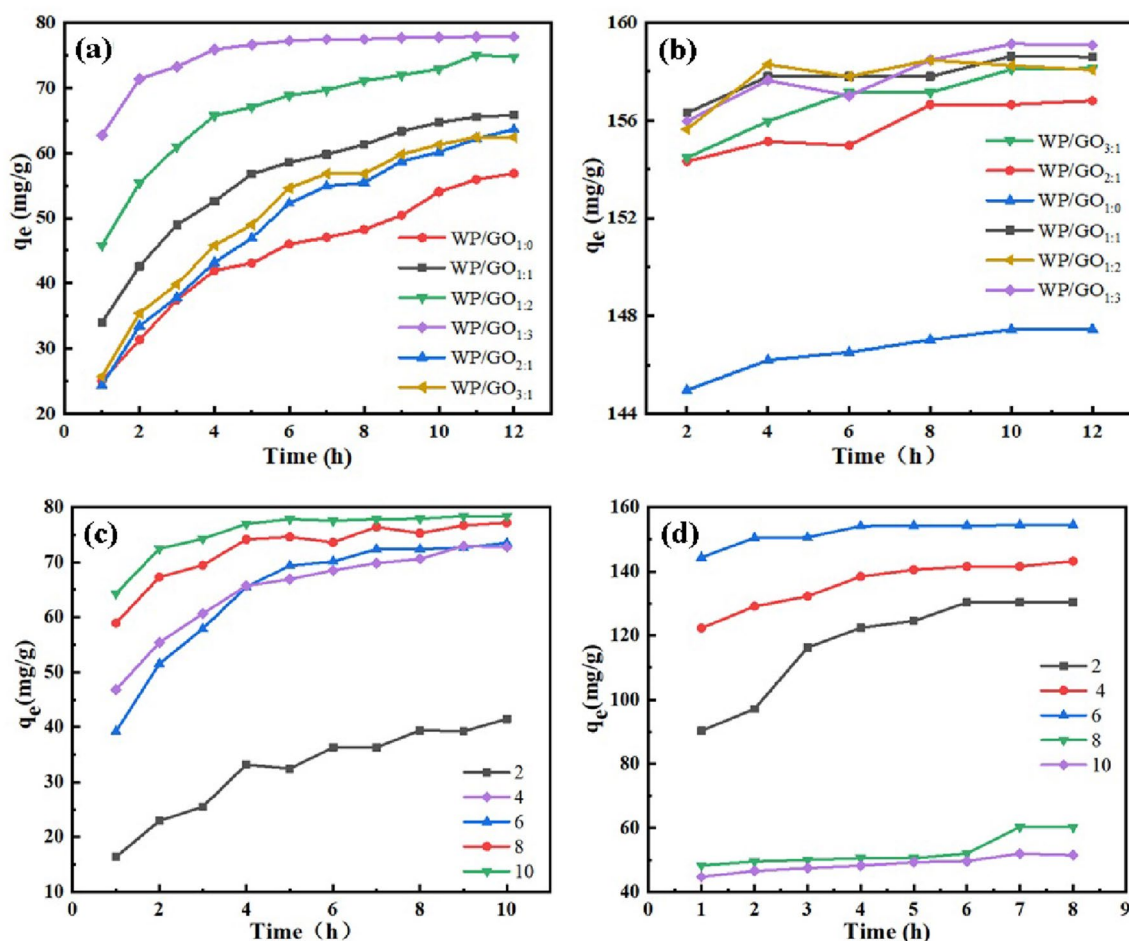
Fig. 8 Effects of adsorption time and mass ratio on adsorption amounts of **a** MB and **b** CIP. Effect of pH on adsorption amounts of **c** MB and **d** CIP

[61]. In addition, the de-protonation of CIP would probably enhance the formation of water cluster around it and inhibit the formation of hydrogen bond between CIP and aerogel, leading to a decrease in the adsorption amount of CIP. Based on the above analysis, the maximum adsorption of CIP could be achieved when CIP existed in the form of zwitterion.

Recycling performance of adsorbent

In Fig. 9a, b, the adsorption capacity of MB by WP/GO$_{1:3}$ aerogel only slightly decreased with increasing the number of adsorption cycle. After the fourth cycle, it reduced from 79.56 to 73.43 mg/g. In Fig. 9c, d, the adsorption capacity of CIP by WP/GO$_{1:3}$ aerogel also declined as the number of adsorption cycle increased. For the first and second cycles, the adsorption amount of CIP changed dramatically. For the third and fourth cycles, it basically did not change. After four cycles, the adsorption capacity of CIP dwindled from 158 to 102 mg/g. However, the removal rate still remained over 65%. These results proved that WP/GO$_{1:3}$ aerogel had

good recycling performance, which might be ascribed that WP/GO$_{1:3}$ aerogel maintained a good network structure after several adsorption cycles.

Adsorption kinetics analysis of binary system

In the solution containing organic dye and antibiotic, the influence of their existence and interaction on the adsorption process needed to be discussed. Thus, the adsorption of MB/CIP binary system was studied.

When CIP was present in binary system (Fig. 10a), the adsorption capacity of MB on WP/GO$_{1:3}$ aerogel increased, stating that CIP had a synergistic effect on MB adsorption. It might be due to the presence of CIP could reduce the electrostatic repulsion between MB and WP/GO$_{1:3}$ aerogel, thereby promoting the adsorption of MB molecule on the surface of aerogel. Nevertheless, when MB was present (Fig. 10b), the adsorption capacity of CIP on WP/GO$_{1:3}$ aerogel reduced, demonstrating that there was a competitive relationship between MB and CIP. In general, the hydrophilic site (e.g.,
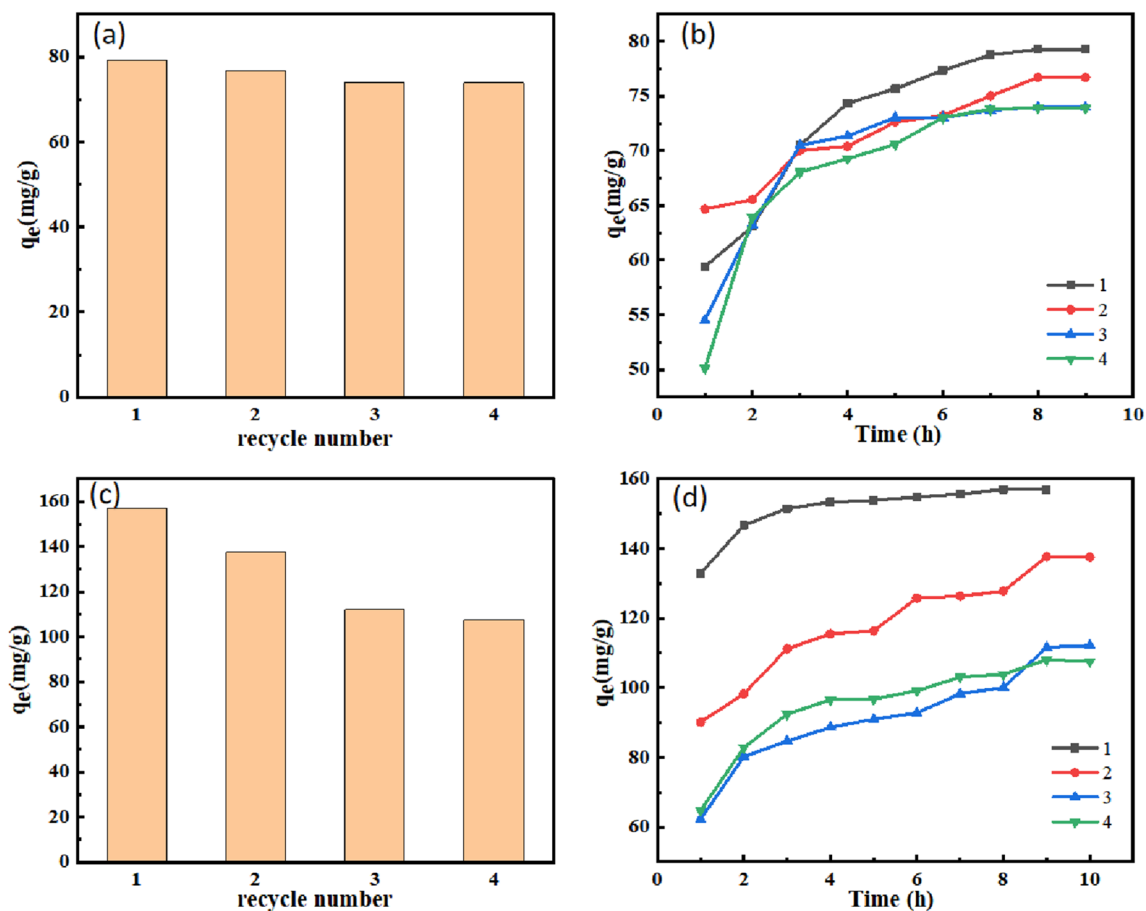
Fig. 9 Cyclic adsorption performance of WP/GO$_{1:3}$ aerogel for **a**, **b** MB and **c**, **d** CIP
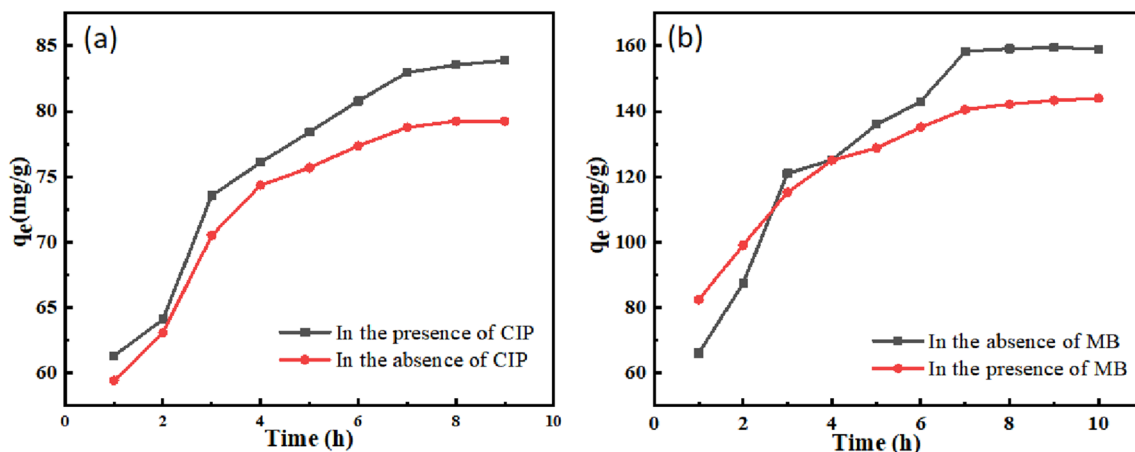

Fig. 10 Adsorption kinetics of **a** MB and **b** CIP by WP/GO$_{1:3}$ aerogel in MB/CIP binary system

–COOH or –OH) could only participate in a kind of chemical interaction, and the affinity with adsorption site of MB was stronger than that of CIP. Accordingly, MB would more quickly occupy the adsorption site than CIP, causing the decrease in CIP adsorption.

According to results in Fig. 11 and Table 4, the correlation coefficients of the pseudo-second-order model equations were both larger than those of the pseudo-first-order model equations for MB and CIP, showing that the pseudo-second-order kinetics was more in line with the adsorption of MB
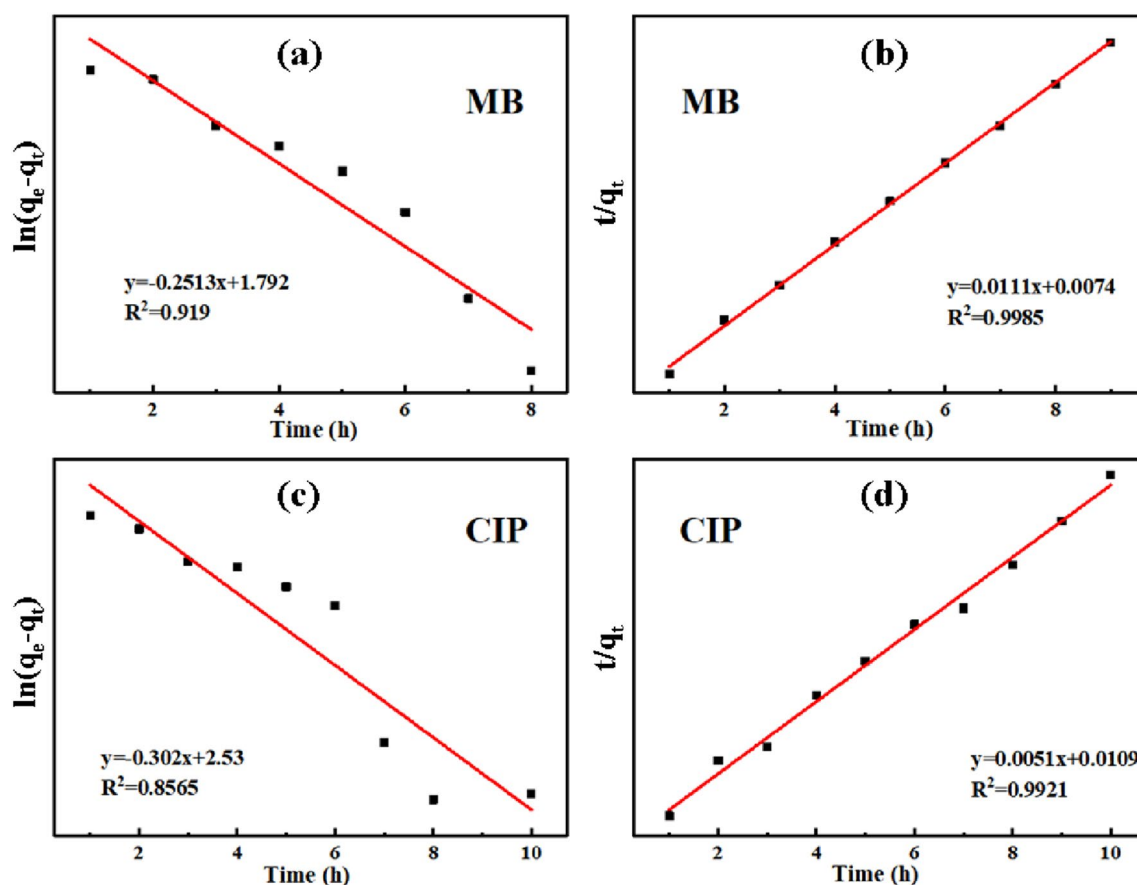
Fig. 11 **a** Pseudo-first-order and **b** pseudo-second-order plots for the adsorption of MB by WP/GO$_{1:3}$ aerogel in MB/CIP binary system. **c** Pseudo-first-order and **d** pseudo-second-order plots for the adsorption of CIP by WP/GO$_{1:3}$ aerogel in MB/CIP binary system

Table 4 Adsorption kinetic parameters for the adsorption of MB and CIP by WP/GO$_{1:3}$ aerogel in MB/CIP binary system

Pollutant	Pseudo-first-order model			Pseudo-second-order model		
	q_e (mg/g)	k_1 (1/h)	R^2	k_2 (mg/g/h^2)	R^2	q_e (mg/g)
MB (in binary system)	61.9441	0.5787	0.919	0.0167	0.9985	90.0900
CIP (in binary system)	338.8441	0.6952	0.8565	0.0024	0.9921	196.0784

and CIP by WP/GO$_{1:3}$ aerogel in MB/CIP binary system. The pseudo-second-order model assumed that the adsorption rate was controlled by chemical adsorption. From this point of view, MB and CIP adsorption by WP/GO$_{1:3}$ aerogel belonged to chemical adsorption, which involved the chemical interactions (e.g., hydrogen bond and π-π conjugation) between hydrophilic functional groups in WP/GO$_{1:3}$ aerogel and MB/CIP.

Adsorption mechanism analysis

Youssef et al. [8] had pointed out that PVA with the characteristics of low price and high quality could act as connective material. Moreover, Hasanin et al. [9] prepared a hybrid material based on extracted porous silica to be

used as adsorbent, where PVA served as a connective biodegradable polymer/a binder polymer. In our work, PVA played the similar role as well. As illustrated in Fig. 12, PVA, GO and WP interacted with each other through hydrogen bonding among –OH, –COOH and C–O, forming aerogel with a tightly hydrogen-bond physical crosslinking network. The adsorption of CIP was realized through the following ways: (1) formation of hydrogen bond (H–F) between –F in CIP and –OH/–COOH in WP/GO$_{1:3}$ aerogel; (2) electrostatic interaction between –NH$^{2\pm}$NH$^+$ in CIP and –COO$^-$ in WP/GO$_{1:3}$ aerogel; (3) π–π conjugated effect between benzene ring in CIP and GO in WP/GO$_{1:3}$ aerogel. On the other hand, the adsorption of MB was acquired through the electrostatic interaction between NH$_3^+$/S$^+$ in MB and –COO$^-$ in WP/GO$_{1:3}$ aerogel and the
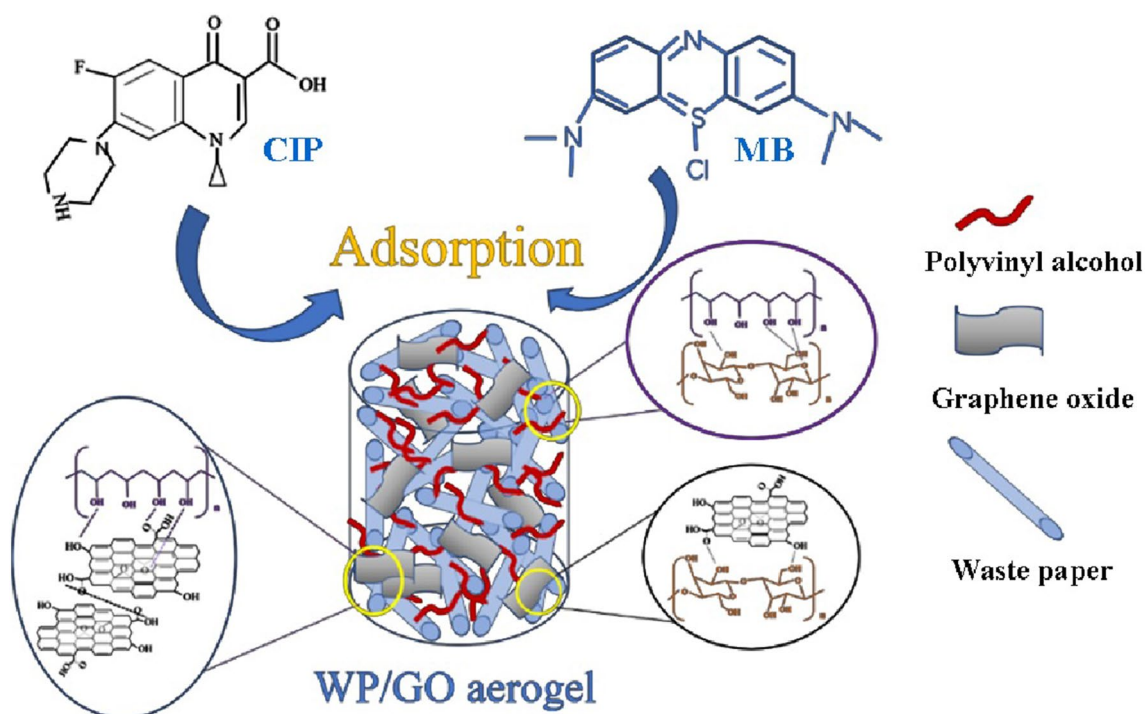
Fig. 12 Schematic illustration of the adsorption mechanism of WP/GO$_{1:3}$ aerogel toward MB and CIP

π–π conjugated effect between benzene rings in MB and WP/GO$_{1:3}$ aerogel.

Conclusions

In summary, a novel three-dimensional aerogel based on GO and WP was prepared via simple mixing and freeze-drying processes. The results showed that the obtained aerogel with improved thermal stability exhibited compact and porous structure, which would supply sufficient adsorption site. The experimental data of adsorption kinetics showed that the pseudo-second-order model was better than the pseudo-first-order model to describe the adsorption of aerogel to MB and CIP. In addition, the adsorption behavior of MB by aerogel was more fitted to the Langmuir isotherm, while the adsorption behavior of CIP by aerogel was more coincided with the Freundlich isotherm. The maximum adsorption capacities of 80 mg/g for MB and 158 mg/g for CIP were achieved. In single system, the adsorption capacity of MB increased steadily while the adsorption capacity of CIP increased first and then decreased, when the solution pH increased from 2 to 10. In binary system, the presence of CIP had a synergistic effect on MB adsorption. The pseudo-second-order kinetics was consistent with the adsorption of pollutant by aerogel. In view of the above, the composite aerogel in this work could be used as an effective, environmental and economical adsorbent for the single or multiple removal of pollutant from environment sewage.

Declarations

Conflict of interest The authors declared that they had no competing financial interest or personal relationship that could appear to affect the work reported in this paper.

References

1. J.J. Yuan, Y.L. Lu, C.C. Wang, X.H. Cao, C.C. Chen, H.T. Cui, M. Zhang, C. Wang, X.Q. Li, A.C. Johnson, A.J. Sweetnnan, D. Du, Ecosyst. Health Sustain. **6**, 1779010 (2020)
2. L.R. Brown, Water Sci. Technol. **43**, 17 (2001)
3. A. Pruss-Ustun, C. Vickers, P. Haefliger, R. Bertollini, Environ. Health **10**, 9 (2011)
4. J.L. Martinez, Environ. Pollut. **157**, 2893 (2009)
5. R.M. Abdelhameed, M. Hasanin, H. Abdel-Gawad, B. Hegazi, Sep. Sci. Technol. **57**, 3023 (2022)
6. A. Abdelkhalek, S.S.M. Ali, Z.W. Sheng, L.L. Zheng, M. Hasanin, Fiber. Polym. **23**, 1171 (2022)
7. A.H. Hashem, E. Saied, M.S. Hasanin, Sustain. Chem. Pharm. **18**, 100333 (2020)

8. N.A. Ibrahim, F.H.H. Abdellatif, M.S. Hasanin, M.M. Abdellatif, J. Clean. Prod. **332**, 130021 (2022)

9. M.S. Hasanin, Environ. Sci. Pollut. Res. **27**, 26742 (2020)

10. G. Abdi, A. Alizadeh, S. Zinadini, G. Moradi, J. Membr. Sci. **552**, 326 (2018)

11. N. Danyliuk, J. Tomaszewska, T. Tatarchuk, J. Mol. Liq. **309**, 113077 (2020)

12. S. De Gisi, G. Lofrano, M. Grassi, M. Notarnicola, Sustain. Mater. Technol. **9**, 10 (2016)

13. K.S. Li, X.Y. Lu, Y. Zhang, K.L. Liu, Y.C. Huang, H. Liu, Environ. Res. **185**, 109409 (2020)

14. Y.C. Huang, H.M. Xu, H.J. Yang, Y. Lin, H. Liu, Y.X. Tong, ACS Sustain. Chem. Eng. **6**, 2751 (2018)

15. J.D. Yang, J.Y. Zhou, Y.C. Huang, Y.X. Tong, ACS Appl. Nano Mater. **5**, 8557 (2022)

16. Y.C. Huang, W.J. Fan, B. Long, H.B. Li, F.Y. Zhao, Z.L. Liu, Y.X. Tong, H.B. Ji, Appl. Catal. B Environ. **185**, 68 (2016)

17. H. Molavi, A. Pourghaderi, A. Shojaei, J. Chem. Eng. Data **64**, 1508 (2019)

18. A.C. Tella, S.O. Owalude, S.J. Olatunji, V.O. Adimula, S.E. Elaigwu, L.O. Alimi, P.A. Ajibade, O.S. Oluwafemi, J. Environ. Sci. **64**, 264 (2018)

19. B.N. Bhadra, I. Ahmed, S. Kim, S.H. Jhung, Chem. Eng. J. **314**, 50 (2017)

20. T. Ngulube, J.R. Gumbo, V. Masindi, A. Maity, J. Environ. Manag. **191**, 35 (2017)

21. S. Ma, S.M. Islam, Y. Shim, Q. Gu, P. Wang, H. Li, G. Sun, X. Yang, M.G. Kanatzidis, Chem. Mater. **26**, 7114 (2014)

22. B. Azambre, M. Chebbi, O. Leroy, L. Cantrel, Ind. Eng. Chem. Res. **57**, 1468 (2018)

23. B. Xin, G. Zeng, L. Gao, Y. Li, S. Xing, J. Hua, G. Li, Z. Shi, S. Feng, Dalton Trans. **42**, 7562 (2013)

24. P. Kuhn, M. Antonietti, A. Thomas, Angew. Chem. Int. Ed. **47**, 3450 (2008)

25. Y. Lan, M. Tong, Q. Yang, C. Zhong, CrystEngComm **19**, 4920 (2017)

26. B.J. Riley, D.A. Pierce, J. Chun, J. Matyas, W.C. Lepry, T.G. Garn, J.D. Law, M.G. Kanatzidis, Environ. Sci. Technol. **48**, 5832 (2014)

27. J. Wang, C. Wang, H. Wang, B. Jin, P. Zhang, L. Li, S. Miao, Microporous Mesoporous Mater. **310**, 110596 (2020)

28. L. Liu, B. Zhang, Y.R. Zhang, Y.J. He, L.H. Huang, S.Z. Tan, X. Cai, J. Chem. Eng. Data **60**, 1270 (2015)

29. Y. Shen, Q.L. Fang, B.L. Chen, Environ. Sci. Technol. **49**, 67 (2015)

30. Z. Sun, S. Fang, Y.H. Hu, Chem. Rev. **120**, 10336 (2020)

31. Z. Wang, H. Gao, Q. Zhang, Y. Liu, J. Chen, Z. Guo, Small **15**, 1803858 (2019)

32. B.Y.Z. Hiew, L.Y. Lee, X.J. Lee, S. Thangalazhy-Gopakumar, S. Gan, S.S. Lim, G.T. Pan, T.C.K. Yang, W.S. Chiu, P.S. Khiew, Process Saf. Environ. **116**, 262 (2018)

33. L. Chen, Y.H. Li, Q.J. Du, Z.H. Wang, Y.Z. Xia, E. Yedinak, J. Lou, L.J. Ci, Carbohydr. Polym. **155**, 345 (2017)

34. X. Xing, W. Jiang, S. Li, X. Zhang, W. Wang, Waste Manag. **89**, 64 (2019)

35. H. Javed, D.X. Luong, C.G. Lee, D. Zhang, J.M. Tour, P.J. Alvarez, Carbon **140**, 441 (2018)

36. C.P. Silva, G. Jaria, M. Otero, V.I. Esteves, V. Calisto, Environ. Sci. Pollut. Res. **26**, 13173 (2019)

37. L.K. Voon, S.C. Pang, S.F. Chin, Carbohydr. Polym. **142**, 31 (2016)

38. P. Dai, Y. Xue, S. Zhang, L. Cao, D. Tang, X. Gu, L. Li, X. Wang, X. Jiang, D. Liu, ACS Appl. Mater. Int. **10**, 37046 (2018)

39. M. Shahrousvand, F.A. Tabar, E. Shahrousvand, A. Babaei, M.M. Hasani-Sadrabadi, G.M.M. Sadeghi, H. Jafari, A. Salimi, Carbohydr. Polym. **175**, 293 (2017)

40. S.T. Nguyen, J. Feng, S.K. Ng, J.P.W. Wong, V.B.C. Tan, H.M. Duong, Colloids Surf. A **445**, 128 (2014)

41. S. Hokkanen, A. Bhatnagar, M. Sillanpaa, Water Res. **91**, 156 (2016)

42. P. Kanmani, J. Aravind, M. Kamaraj, P. Sureshbabu, S. Karthikeyan, Bioresour. Technol. **242**, 295 (2017)

43. N.I. Kovtyukhova, P.J. Ollivier, B.R. Martin, T.E. Mallouk, S.A. Chizhik, E.V. Buzaneva, A.D. Gorchinskiy, Chem. Mater. **11**, 771 (1999)

44. J.L. Zhang, H.D. Liu, P. Shi, Y.J. Li, L.H. Huang, W.J. Mai, S.Z. Tan, X. Cai, J. Power Sources **267**, 356 (2014)

45. T. Szabo, O. Berkesi, I. Dekany, Carbon **43**, 3186 (2005)

46. H. Abral, A. Hartono, F. Hafizulhaq, D. Handayani, E. Sugiarti, O. Pradipta, Carbohydr. Polym. **206**, 593 (2019)

47. Y. Guan, Y. Bian, F. Peng, X.M. Zhang, R.C. Sun, Carbohydr. Polym. **101**, 272 (2014)

48. H. Dai, S. Ou, Z. Liu, H. Huang, Carbohydr. Polym. **169**, 504 (2017)

49. H.D. Liu, J.L. Zhang, B. Zhang, L. Shi, S.Z. Tan, L.H. Huang, Electrochim. Acta **138**, 69 (2014)

50. K.H. Ye, Y. Li, H. Yang, M.Y. Li, Y.C. Huang, S.Q. Zhang, H.B. Ji, Appl. Catal. B Environ. **259**, 118085 (2019)

51. S. Stankovich, D.A. Dikin, R.D. Piner, K.A. Kohlhaas, A. Kleinhammes, Y. Jia, Y. Wu, S.T. Nguyen, R.S. Ruoff, Carbon **45**, 1558 (2007)

52. W. Zhu, T. Chen, Y. Li, J. Lei, X. Chen, W. Yao, T. Duan, Materials **10**, 536 (2017)

53. A. Donia, A. Atia, F. Abouzayed, Chem. Eng. J. **191**, 22 (2012)

54. J. Li, G. Yu, L. Pan, C. Li, F. You, S. Xie, Y. Wang, J. Ma, X. Shang, J. Environ. Sci. **73**, 20 (2018)

55. T. Ma, P.R. Chang, P. Zheng, F. Zhao, X. Ma, Chem. Eng. J. **240**, 595 (2014)

56. L. Mouni, L. Belkhiri, J.C. Bollinger, A. Bouzaza, A. Assadi, A. Tirri, F. Dahmoune, K. Madani, H. Remini, Appl. Clay Sci. **153**, 38 (2018)

57. Y. Liu, M. Liu, J. Jia, D. Wu, T. Gao, X. Wang, J. Yu, F. Li, Nanoscale **11**, 18653 (2019)

58. W. Wang, Y. Zhao, H. Bai, T. Zhang, V. Ibarra-Galvan, S. Song, Carbohydr. Polym. **198**, 518 (2018)

59. J. Xu, Y.Y. Hu, X.Y. Li, J.J. Chen, G.P. Sheng, Environ. Pollut. **243**, 752 (2018)

60. X. Peng, F. Hu, F.L. Lam, Y. Wang, Z. Liu, H. Dai, J. Colloid Interface Sci. **460**, 349 (2015)

61. N. Genc, E.C. Dogan, Desalin. Water Treat. **53**, 785 (2015)